2016

Hydrogen-induced ferromagnetism in two-dimensional Pt dichalcogenides

P. Manchanda
University of Nebraska - Lincoln

Axel Enders
University of Nebraska - Lincoln, a.enders@me.com

David J. Sellmyer
University of Nebraska-Lincoln, dsellmyer@unl.edu

Ralph Skomski
University of Nebraska-Lincoln, rskomski2@unl.edu

Hydrogen-induced ferromagnetism in two-dimensional Pt dichalcogenides

P. Manchanda, A. Enders, D. J. Sellmyer, and R. Skomski
Department of Physics and Astronomy and Nebraska Center for Materials and Nanoscience, University of Nebraska, Lincoln, Nebraska 68588, USA
(Received 11 April 2016; revised manuscript received 20 July 2016; published 23 September 2016)

Electronic, structural, and magnetic properties of Pt dichalcogenide monolayers are investigated using first-principle calculations. We find that hydrogenation lifts the spin degeneracy in narrow antibonding Pt 5*d* subband electrons and transforms the nonmagnetic semiconductors PtX_2 (X = S,Se,Te) into ferromagnetic metals, PtX_2-1H; neither strain nor thin-film edges are necessary to support the transition. The trend towards ferromagnetism is most pronounced for X = S, decreasing with increasing atomic weight of the chalcogens.

DOI: 10.1103/PhysRevB.94.104426

I. INTRODUCTION

Two-dimensional (2D) materials, including graphene, boron nitride, and transition-metal dichalcogenides are important candidates for new electronic devices, because they combine desirable electronic properties, such as low effective mass, high carrier mobilities, and electronic band gaps of practical magnitude, while at the same time having the potential for synthesis [1–5]. Two-dimensional materials are expected to enable new low-dimensional, cheap, and flexible nanoelectronics for memory, logic, and information processing architectures, extending microelectronics beyond the 2011 International Technology Roadmap for Semiconductors, ITRS. In particular, as traditional complementary metal-oxide semiconductor (CMOS) scaling reaches its spatial limits, there is immense interest in the development of novel *non-charge*-based devices to enable significant functional scaling of logic circuits [6,7]. One example of a promising 2D material is MoS_2 [8–11], which exhibits a moderate band gap of about 1.80 eV [12], a reasonable carrier mobility of 200 $cm^2\,V^{-1}\,s^{-1}$ though much lower than that of GaAs quantum wells [13] a very good ON-OFF current ratio [8], and excellent electrostatic integrity [14,15]. The existence of a band gap sets MoS_2 apart from the gapless graphene, enabling a defined OFF state in logic devices, [11], which is a major drawback in graphene-based applications.

Two-dimensional transition-metal dichalcogenides (TMDs) have the chemical composition TX_2 (T = transition metal, X = S,Se,Te). Depending on the number of transition-metal d electrons and on the chalcogen-ligand environment, they often exhibit insulating, metallic, superconducting, and charge-density-wave electronic structures [8,16–18]. However, most 2D TMDs, for example, MoS_2 and WSe_2, are nonmagnetic semiconductors.

Recent materials-by-design strategies aim at expanding the functionality of 2D materials, for instance, by introducing electric and magnetic polarization. These strategies exploit the unique amenability of 2D materials to chemical doping [11,19], external electric fields [20–22], mechanical strain [22–24], and chemical surface functionalization with adatoms such as hydrogen or fluorine [25–29]. The effect of surface hydrogenation on magnetic anisotropy is well established for 3*d* metals [30], and hydrogenation appears to be a viable route to manipulate the magnetic properties of TMDs as well: Hydrogenation has been predicted to modify the ferromagnetism of VS_2,VSe_2, and VTe_2 monolayers [26,28]. Loh *et al.* used first-principle calculations to predict ferromagnetism in fluorinated semiconducting ReS_2 monolayers [29], and a small magnetic moment of 0.06 emu/g is observed in fluorinated MoS_2 nanosheets [31].

The emergence of magnetic moments in TMDs is of particular interest, because it is the fundamental atomic basis for ferromagnetism. In this context, the effects of edges in graphene and nanoribbons are well known [32–34]. Hydrogenation has been predicted to yield ferromagnetism in MoS_2 monolayers, but only in the simultaneous presence of biaxial strain [27]. Hydrogenation of armchair MoS_2 and WS_2 nanoribbons has been reported to transform the ribbons into ferromagnetic semiconductors [35,36], which was also predicted for $SnSe_2$ [37]. While enhanced interatomic distances and reduced coordination at edges tend to favor ferromagnetism in general, more research is needed on the ability of straightforward hydrogenation to transform a nonmagnetic TMD into a ferromagnetic TMD.

Our focus is on monolayers of PtX_2 (X = S,Se,Te). Compared to the widely studied Mo and W TMDs, PtS_2 and $PtSe_2$ [38–40] attracted relatively little attention at first due to the high materials cost of Pt. However, recent experimental progress in the synthesis of $PtSe_2$ monolayers [41] has sparked renewed interest in Pt (and Pd) chalcogenides [42–44]. Like the corresponding bulk materials, the monolayers are nonmagnetic semiconductors, which leads to the question whether and how these films can be made magnetic. In this paper, we use first-principle calculations to investigate electronic and magnetic properties of PtX_2 (X = S,Se,Te) monolayers and predict that hydrogenation introduces ferromagnetism in PtX_2 monolayers.

II. COMPUTATIONAL DETAILS

The density-functional theory (DFT) calculations were carried out using the projector augmented wave (PAW) method [45], as implemented in the Vienna *ab initio* simulation package (VASP) [46,47]. Within the generalized gradient approximation (GGA), we employed Perdew-Burke-Ernzerhof (PBE) exchange and correlation functionals [48]. The electron wave function was expanded in a planewave basis set with an energy cutoff of 520 eV, and a Γ-centered 23 × 23 × 1 k mesh was used to sample the Brillouin zone (BZ) for electronic structure and density of states calculations [49]. All the

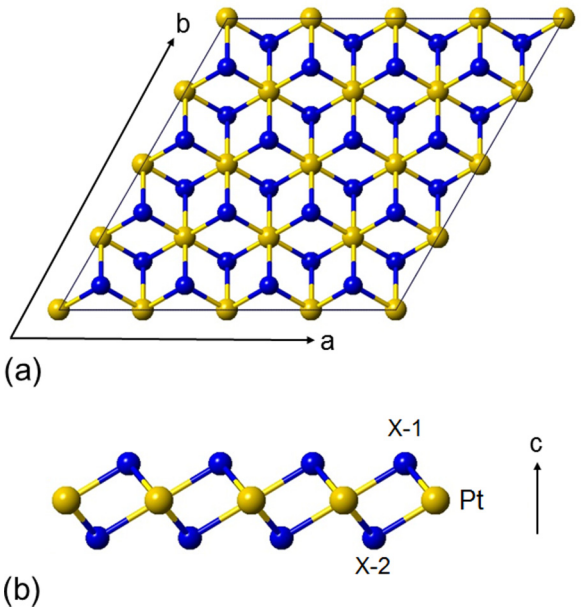

FIG. 1. Atomic structure of monolayers of 1T PtX_2(X = S,Se,Te): (a) top view and (b) side view.

atomic structures were fully relaxed until the force on each atom was less than 0.002 eV/Å, and the energy-convergence criterion was 1×10^{-6}eV. To investigate the spin structure, we constructed a $4 \times 4 \times 1$ supercell, and a sufficently large vacuum space of about 20 Å was used in the vertical direction to avoid the interaction between neighboring supercells. For the total-energy calculations of the various spin structures, $11 \times 11 \times 1\,k$ mesh was used. Figure 1 shows top and side views of the considered 1T platinum dicalcogenide monolayers (PtX_2, X = S,Se,Te). We have also performed highly accurate electronic-structure calculations using the screened-nonlocal-exchange Heyd-Scuseria-Ernzerhof (HSE) hybrid functional [50,51]. The screening parameter in HSE is fixed at a value of 0.2 $Å^{-1}$.

III. RESULTS

We have considered PtX_2 monolayers, with the focus on the effect of hydrogenation when one surface of the PtX_2 monolayer is covered by hydrogen atoms (PtX_2-H). Bulk and

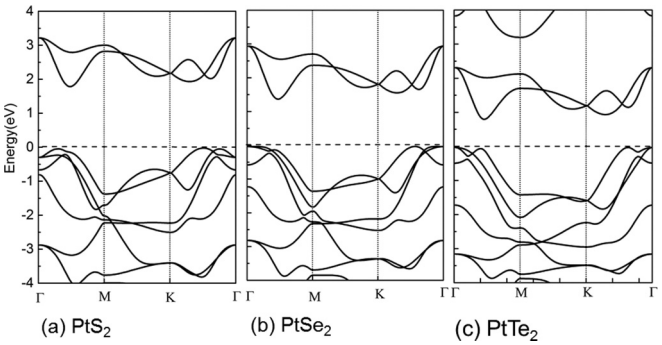

FIG. 2. Calculated band structures of the monolayers: (a) PtS_2, (b) $PtSe_2$, and (c) $PtTe_2$. The dashed line indicates the Fermi level.

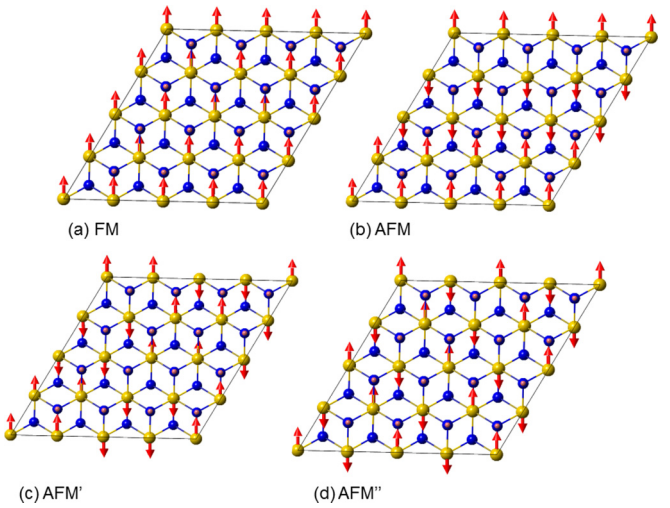

FIG. 3. Different spin configurations in PtH_2-1H: (a) ferromagnetic and (b)–(d) antiferromagnetic. For simplicity, all calculations have been performed for a $4 \times 4 \times 1$ supercell.

monolayer PtX_2 are well known to crystallize in 1T form shown in Fig. 1 [52,53]. Our respective optimized lattice parameters of uncovered PtS_2, $PtSe_2$, and $PtTe_2$ monolayers, namely, 3.57, 3.77, and 4.08 Å, are consistent with previous results [42]. The band structure calculated using the PBE functional (Fig. 2) shows that the PtS_2, $PtSe_2$, and $PtTe_2$ monolayers are semiconductors with indirect band gaps of 1.80, 1.40, and 0.70 eV, respectively. In all three films, the conduction-band minimum (CBM) is located halfway between the Γ and M points. In the PtS_2 monolayer, the valence-band maximum (VBM) is located between the K and Γ high-symmetry points, whereas in the $PtSe_2$ and $PtTe_2$ monolayers, the VBM is located at the Γ point. In all three films, the CBM and VBM are mainly dominated by X-p and Pt-d electrons. The monolayer band gaps from the HSE calculations, 2.50 eV (PtS_2), 2.00 eV ($PtSe_2$), and 1.20 eV ($PtTe_2$) (see Fig. S1 in the Supplemental Material [54]), are in very good agreement with the optical gap [44,55].

Figure 3 shows the considered hydrogenated PtX_2 monolayers, where one surface (X-1) is covered by hydrogen atoms and the other one (X-2) remains unsaturated. For the hydrogenation, there are two possible positions, namely, on top of Pt and on top of X-1. We find the latter site more favorable for hydrogen adsorption and used it for the calculations in the present paper. Table I shows the optimized lattice parameters and absorption energies. Our respective lattice parameters are obtained by volume optimization. The hydrogenation causes the PtX_2 monolayer lattices to expand: For S_1-H,Se_1-H, and

TABLE I. Lattice parameters and energies of PtX_2 monolayers whose X-1 surface is covered by hydrogen.

	a (Å)	$d_{Pt\text{-}X1}$(Å)	$d_{Pt\text{-}X2}$(Å)	$d_{X1\text{-}H}$(Å)	E_a(eV)
PtS_2-H	3.77	2.43	2.48	1.38	–1.142
$PtSe_2$-H	3.94	2.55	2.61	1.54	–1.081
$PtTe_2$-H	4.16	2.71	2.79	1.76	–1.042

TABLE II. Magnetism of the hydrogenated monolayers: monolayer energies relative to the ferromagnetic state (columns 2–5) and the corresponding magnetic moments per atom (columns 6–8).

	E_{FM}(eV)	E_{AFM}(meV)	$E_{AFM'}$(meV)	$E_{AFM''}$(meV)	Pt(μ_B)	X-1(μ_B)	X-2(μ_B)
PtS_2-H	0	14.37	14.83	22.0	0.357	0.059	0.174
$PtSe_2$-H	0	15.01	14.75	21.72	0.293	0.043	0.17
$PtTe_2$-H	0	4.20	3.95	3.95	0.175	0.033	0.11

Te_1-H, the respective bond lengths are 1.38, 1.54, and 1.76 Å. The energy per adsorbed hydrogen atom has been calculated as [27]

$$E_a = E_{tot}(PtX_2 + H) - E_{tot}(PtX_2) - E(H), \quad (1)$$

where $E_{tot}(PtX_2 + H)$ and $E_{tot}(PtX_2)$ are the total energies of hydrogenated PtX_2 and pure PtX_2, respectively, and $E(H)$ is the energy of the hydrogen atom.

To study the magnetic ground state of the hydrogenated PtX_2 monolayers, we have calculated the total energies of the four (anti)ferromagnetic spin configurations shown in Fig. 3. Table II lists the energies per unit cell relative to the ferromagnetic (FM) state. In all three structures (PtS_2-1H, $PtSe_2$-1H, $PtTe_2$-1H), the ground state is ferromagnetic. The Curie temperature reflects the energy per broken (or antiferromagnetic) exchange bond relative to the ferromagnetic state. Mean-field theory provides a Curie temperature estimate of $T_c = (2/3)\, E_{ex}/k_B$ [56]. For PtS_2-1H and $PtSe_2$-1H, this yields a Curie temperature of 170 and 168 K, respectively. We have chosen the AFM″ state to determine T_c, but the other two spin configurations yield similar results, because they contain fewer antiferromagnetic bonds per supercell.

The nonmonotonic behavior of the exchange energy as a function of the atomic number of the chalcogenide (Table II) is a size effect. Exchange involves the overlap of wave functions, and the bigger size of the heavier atoms leads to larger interatomic distances, reduced overlap, and reduced magnitude of exchange. This dependence mirrors the above-mentioned structural trend (bond lengths), because both phenomena involve interatomic exchange.

It is interesting to pinpoint the origin of the magnetic moment in real space and in k space. Figure 4 shows the calculated real-space spin-density distribution in the PtS_2-1H monolayer. The magnetism mainly originates from 5d orbitals of the Pt atoms, but there is also a substantial contribution localized around the unsaturated S-2 atoms ($0.17\mu_B$), largely stemming from the S-2 $3p_z$ orbitals. The hydrogenated S-1 and H atoms carry a very small magnetic moment (altogether $0.06\,\mu_B$), mainly originating from the 3s orbitals of the S-1 atoms. Similar spin-density distributions have been found in the $PtSe_2$-1H and $PtTe_2$-1H monolayers. As we can see from Table II, Pt has magnetic moments of 0.357, 0.293, and $0.175\mu_B$ in hydrogenated PtS_2, $PtSe_2$, and $PtTe_2$ monolayers, respectively. While these moments are rather modest, they are likely to create big spin-orbit effects, whose investigation is a challenge to future research.

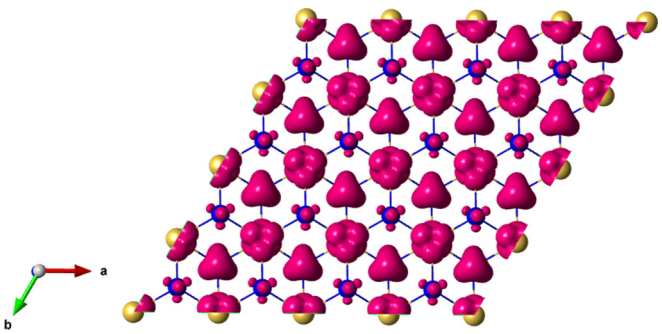

FIG. 4. Spin-density distribution: Top view on a spin-density isosurface of a ferromagnetic monolayer of PtS_2-1H.

The k-space origin of the moment is evident from band dispersions of Fig. 5. The hydride monolayers are metallic, and the spin-up bands lie below the spin-down bands, both having similar distributions in reciprocal space. From the densities of states, Fig. 6, we see that the onset of itinerant ferromagnetism corresponds to the splitting of a narrow subband near the Fermi level, which is empty in the PtX_2 monolayers but partially filled in the hydrides. This mechanism is a unique feature of the TMD structure: The partially filled subband is predominantly formed from Pt $5d_{xz}$ and $5d_{yz}$ orbitals, which have substantial in-plane (x,y) and perpendicular (z) real-space components, as contrasted to the in-plane $5d_{xy}$, $5d_{x^2-y^2}$ orbitals and to the perpendicular $5d_{z^2}$ orbital. The $5d_{xz}$ and $5d_{yz}$ orbitals therefore undergo a strong hybridization with the orbitals of the X nearest neighbors, which are not located in the Pt plane but at an oblique angle (Fig. 1). This creates a hybridization gap and an antibonding band near the Fermi level.

Additional hydrogen coverage of the *second* surface (X-2) destroys the magnetic moment, because the extra hydrogen fills the Pt 5d peak near the Fermi level. The hydrogen coverage of the second surface is a rather extreme limit, because thin films are normally deposited on surfaces that do not exhibit this harmful band-filling effect. However, the explicit

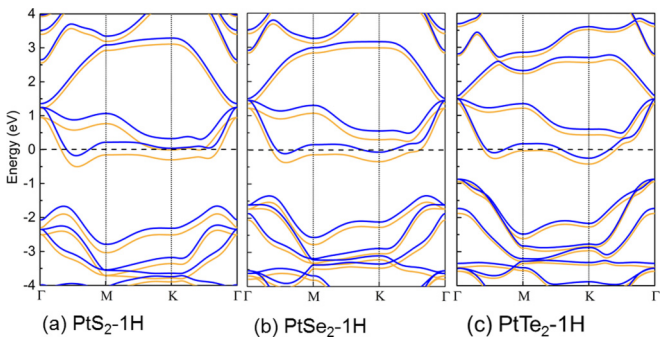

FIG. 5. Calculated monolayer band structures along high-symmetry directions: (a) PtS_2-1H, (b) $PtSe_2$-1H, and (c) $PtTe_2$-1H. The orange and blue lines represent spin-up and spin-down bands, respectively.

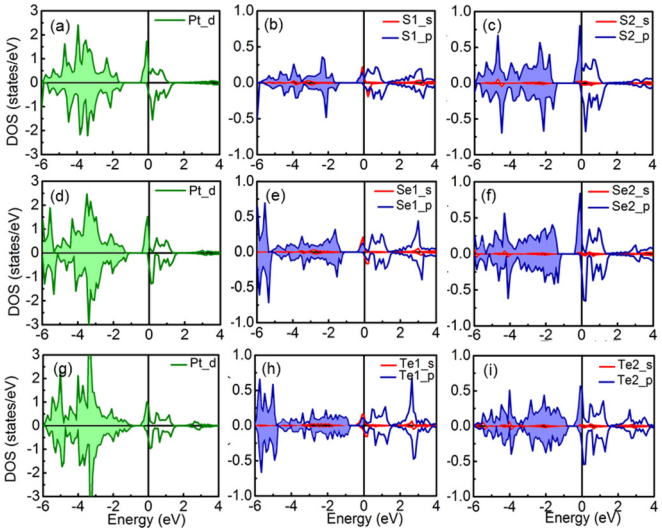

FIG. 6. Calculated spin-polarized partial density of states: (a)–(c) PtS_2-1H, (d)–(f) $PtSe_2$-1H, and (g)–(i) $PtTe_2$-1H.

investigation of PtX_2 monolayers and the corresponding zero- and finite-temperature magnetic and transport properties (including carrier mobility) go far beyond the scope of the present paper and remain a challenge to future research.

Using HSE calculations, we find that PtX_2-H remains spin polarized with magnetic moments increased as compared to PBE. This is attributed to the smaller hybridization between Pt-d and X-p orbitals, as the GGA scheme tends to overestimate the stability of delocalized states due to the self-interaction energy. Interestingly, we find that PtS_2-1H monolayers become half-metallic with the total magnetic moment of $1\mu_B$/unit cell. By comparing the total DOS of PtS_2-H (see Fig. S2 of the Supplemental Material [54]) using PBE and HSE calculations, we find that minority states move downwards from the Fermi level, which leads to *half-metallic* spin structures. It is, therefore, confirmed that our results of induced ferromagnetism in PtX_2 monolayers with hydrogenation are robust irrespective of the choice of DFT functional.

IV. CONCLUSIONS

In summary, we have used spin-polarized density-functional theory to study the stability, electronic, and magnetic properties of hydrogenated PtS_2, $PtSe_2$, and $PtTe_2$ monolayers. We find that hydrogenation transforms the semiconducting PtX_2 monolayers into ferromagnetic metals whose magnetic moment mainly originates from Pt 5d electrons which are spin polarized through a narrow antibonding subband. Both the trend towards ferromagnetism and the structural stability of the hydrides decrease with increasing chalcogen atomic number, being most pronounced for PtS_2. Our research indicates that hydrogenation of heavy-transition-metal dichalcogenides may be an effective tool to design the properties of two-dimensional materials by introducing ferromagnetism.

ACKNOWLEDGMENTS

This work has been supported by ARO (Grant No. W911NF-10-2-0099, P.M.), and DOE BES (Grant No. DE-FG02-04ER46152, R.S. and D.J.S.). The computations were performed at the University of Nebraska Holland Computing Center. The authors are thankful to Jingtian Fang for the helpful discussions.

[1] J. N. Coleman, M. Lotya, A. O'Neill, S. D. Bergin, P. J. King, U. Khan, K. Young, A. Gaucher, S. De, R. J. Smith, I. V. Shvets, S. K. Arora, G. Stanton, H. Y. Kim, K. Lee, G. T. Kim, G. S. Duesberg, T. Hallam, J. J. Boland, J. J. Wang *et al.*, Science **331**, 568 (2011).
[2] X. Zhang and Y. Xie, Chem. Soc. Rev. **42**, 8187 (2013).
[3] M. Fontana, T. Deppe, A. K. Boyd, M. Rinzan, A. Y. Liu, M. Paranjape, and P. Barbara, Sci. Rep. **3**, 1634 (2013).
[4] S. Z. Butler, S. M. Hollen, L. Cao, Y. Cui, J. A. Gupta, H. R. Gutiérrez, T. F. Heinz, S. S. Hong, J. Huang, A. F. Ismach, E. Johnston-Halperin, M. Kuno, V. V Plashnitsa, R. D. Robinson, R. S. Ruoff, S. Salahuddin, J. Shan, L. Shi, M. G. Spencer, M. Terrones *et al.*, ACS Nano **7**, 2898 (2013).
[5] S. Das, R. Gulotty, A. V. Sumant, and A. Roelofs, Nano Lett. **14**, 2861 (2014).
[6] International Technology Roadmap for Semiconductors, Chapter PIDS, 2011, available online at http://www.itrs2.net/2011-itrs.html.
[7] J. Fang, W. G. Vandenberghe, B. Fu, and M. V. Fischetti, J. Appl. Phys. **119**, 035701 (2016).
[8] B. Radisavljeic, A. Radenovic, J. Brivio, V. Giacometti, and A. Kis, Nat. Nanotechnol. **6**, 147 (2011).
[9] R. F. Service, Science **348**, 490 (2015).
[10] H. Wang, H. Yuan, S. S. Hong, Y. Li, and Y. Cui, Chem. Soc. Rev. **44**, 2664 (2014).
[11] B. Radisavljevic and A. Kis, Nat. Mater. **12**, 815 (2013).
[12] K. F. Mak, C. Lee, J. Hone, J. Shan, and T. F. Heinz, Phys. Rev. Lett. **105**, 136805 (2010).
[13] K.-J. Friedland, R. Hey, H. Kostial, R. Klann, and K. Ploog, Phys. Rev. Lett. **77**, 4616 (1996).
[14] Y. Yoon, K. Ganapathi, and S. Salahuddin, Nano Lett. **11**, 3768 (2011).
[15] K. Alam, and R. K. Lake, IEEE Trans. Electron Devices **59**, 3250 (2012).
[16] D. Jariwala, V. K. Sangwan, L. J. Lauhon, T. J. Marks, and M. C. Hersam, ACS Nano **8**, 1102 (2014).
[17] J. T. Ye, Y. J. Zhang, R. Akashi, M. S. Bahramy, R. Arita, and Y. Iwasa, Science **338**, 1193 (2012).
[18] X. Xi, L. Zhao, Z. Wang, H. Berger, L. Forró, J. Shan, and K. F. Mak, Nat. Nanotechnol. **10**, 765 (2015).
[19] P. Manchanda and R. Skomski, J. Phys.: Condens. Matter **28**, 064002 (2016).
[20] S. Wu, J. S. Ross, G.-B. Liu, G. Aivazian, A. Jones, Z. Fei, W. Zhu, D. Xaio, W. Yao, D. Cobden, and X. Xu, Nat. Phys. **9**, 149 (2013).
[21] H. Rostami, A. G. Moghaddam, and R. Asgari, Phys. Rev. B **88**, 085440 (2013).
[22] Y. Zhou, Z. Wang, P. Yang, X. Zu, L. Yang, X. Sun, and F. Gao, ACS Nano **6**, 9727 (2012).

[23] P. Manchanda, V. Sharma, H.-B. Yu, D. J. Sellmyer, and R. Skomski, Appl. Phys. Lett. **107**, 032402 (2015).
[24] Y. Ma, Y. Dai, M. Guo, C. Niu, Y. Zhu, and B. Huang, ACS Nano **6**, 1695 (2012).
[25] C. Ataca and S. Ciraci, J. Phys. Chem. C **115**, 13303 (2011).
[26] H. Pan, J. Phys. Chem. C **118**, 13248 (2014).
[27] H. Shi, H. Pan, Y.-W. Zhang, and B. I. Yakobson, Phys. Rev. B **88**, 205305 (2013).
[28] H. Pan, Sci. Rep. **4**, 7524 (2014).
[29] G. C. Loh and R. Pandey, Phys. Chem. Chem. Phys. **17**, 18843 (2015).
[30] D. Sander, W. Pan, S. Ouazi, J. Kirschner, W. Meyer, M. Krause, S. Müller, L. Hammer, and K. Heinz, Phys. Rev. Lett. **93**, 247203 (2004).
[31] D. Gao, S. Shi, K. Tao, B. Xia, and D. Xue, Nanoscale **7**, 4211 (2015).
[32] Y. Li, Z. Zhou, S. Zhang, and Z. Chen, J. Am. Chem. Soc. **130**, 16739 (2008).
[33] Z. Zhang, X. Zou, V. H. Crespi, and B. I. Yakobson, ACS Nano **7**, 10475 (2013).
[34] N. Huo, Y. Li, J. Kang, Q. Xia, and J. Li, Appl. Phys. Lett. **104**, 202406 (2014).
[35] F. Ouyang, Z. Yang, X. Ni, N. Wu, Y. Chen, and X. Xiong, Appl. Phys. Lett. **104**, 071901 (2014).
[36] F. Ouyang, X. Ni, Z. Yang, Y. Chen, X. Zheng, and X. Xiong, J. Appl. Phys. **114**, 213701 (2013).
[37] Y. Huang, C. Ling, H. Liu, and S. Wang, J. Mater. Chem. C **2**, 10175 (2014).
[38] F. Grønvold and E. Rost, Acta Chem. Scand. **10**, 1620 (1956).
[39] A. Kjekshus and F. Grønvold, Acta Chem. Scand. **13**, 1767 (1959).
[40] J. A. Wilson and A. D. Yoffe, Adv. Phys. **18**, 193 (1969).
[41] Y. Wang, L. Li, W. Yao, S. Song, J. T. Sun, J. Pan, X. Ren, C. Li, E. Okunishi, Y.-Q. Wang, E. Wang, Y. Shao, Y. Y. Zhang, H.-T. Yang, E. F. Schwier, H. Iwasawa, K. Shimada, M. Taniguchi, Z. Cheng, S. Zhou *et al.*, Nano Lett. **15**, 4013 (2015).
[42] P. Miró, M. Ghorbani-Asl, and T. Heine, Angew. Chem., Int. Ed. **53**, 3015 (2014).
[43] J. Sun, H. Shi, T. Siegrist, and D. J. Singh, Appl. Phys. Lett. **107**, 153902 (2015).
[44] Y. Wang, Y. Li, and Z. Chen, J. Mater. Chem. C **3**, 9603 (2015).
[45] G. Kresse and D. Joubert, Phys. Rev. B **59**, 1758 (1999).
[46] G. Kresse and J. Hafner, Phys. Rev. B **47**, 558 (1993).
[47] G. Kresse and J. Furthmüller, Comput. Mater. Sci. **6**, 15 (1996).
[48] J. P. Perdew, K. Burke, and M. Ernzerhof, Phys. Rev. Lett. **77**, 3865 (1996).
[49] H. J. Monkhorst and J. D. Pack, Phys. Rev. B **13**, 5188 (1976).
[50] H. Heyd, G. Scuseria, and M. Ernzerhof, J. Chem. Phys. **118**, 8207 (2003).
[51] F. Fuchs, J. Furthmüller, F. Bechstedt, M. Shishkin, and G. Kresse, Phys. Rev. B **76**, 115109 (2007).
[52] M. J. Piotrowski, R. K. Nomiyama, and J. L. F. Da Silva, Phys. Rev. B **88**, 075421 (2013).
[53] F. A. Rasmussen and K. S. Thygesen, J. Phys. Chem. C **119**, 13169 (2015).
[54] See Supplemental Material at http://link.aps.org/supplemental/10.1103/PhysRevB.94.104426 for the electronic structure of PtX_2 and hydrogenated PtX_2 using HSE functional.
[55] H. L. Zhuang and R. G. Hennig, J. Phys. Chem. C **117**, 20440 (2013).
[56] J. Kudrnovský, I. Turek, V. Drchal, F. Máca, P. Weinberger, and P. Bruno, Phys. Rev. B **69**, 115208 (2004).